We are IntechOpen, the world's leading publisher of Open Access books Built by scientists, for scientists

4,800
Open access books available

122,000
International authors and editors

135M
Downloads

Our authors are among the

154
Countries delivered to

TOP 1%
most cited scientists

12.2%
Contributors from top 500 universities

CLARIVATE ANALYTICS BOOK CITATION INDEX INDEXED

WEB OF SCIENCE™

Selection of our books indexed in the Book Citation Index in Web of Science™ Core Collection (BKCI)

Interested in publishing with us?
Contact book.department@intechopen.com

Numbers displayed above are based on latest data collected.
For more information visit www.intechopen.com

11

Synthesis, Sintering Behaviour and Mechanical Properties of Lead-Ceramic (Nano-)Composites for Acid Battery Grids

Alexandre Maître[1] and Michel Vilasi[2]
[1]*Laboratoire Science des Procédés Céramiques et de Traitements de Surface – UMR CNRS 6638 – Centre Européen de la Céramique – 12 rue Atlantis F-87068 Limoges Cedex*
[2]*Institut Jean Lamour – UMR CNRS 7555 – Faculté des Sciences et Techniques – Boulevard des Aiguillettes – F-54506 Vandœuvre-lès-Nancy Cedex*
France

1. Introduction

In recent years, lead-calcium-tin alloys have been widely used for producing lead/acid battery grids. In particular, lead-calcium-tin grids are usually employed for the positive grids of Valve-Regulated Lead Acid batteries (VRLA) or maintenance free storage lead/acid batteries (Giess, 1995 ; Bagshaw, 1995). Indeed, Pb-Ca-Sn alloys present better mechanical and electrochemical properties considering Pb-Ca or Pb-Sb systems. In particular, the addition of tin to lead-calcium alloys dramatically improves the conductivity of corrosion products on the grid surface, allowing improved corrosion resistance and inhibition of the formation of non conductive layers at the grid-active material interface (Miraglio et al., 1995; Takahashi et al., 1995). Furthermore, tin increases the resistance corrosion in overcharge conditions because it leads to the rising of the oxygen overvoltage (Bui et al., 1997).
From a metallurgical point of view, the age-hardening process of the most commonly used ternary alloys Pb-Ca(0.08wt.%)Sn(2wt.%) proceeds by discontinuous or continuous precipitation of $L1_2$ phase (*i.e.* $(Pb_{1-x}Sn_x)_3Ca$) from supersaturated α solid solution (Maître et al., 2003 ; Bouirden et al., 1991). Moreover, at room temperature, the residual tin and calcium supersaturation of aged ternary alloys can lead to the overageing appearance. The overageing process of Pb-Sn alloys takes place in two stages (Maître et al., 2003): first, a discontinuous precipitation of a coarse $L1_2$ phase, second, the lamellar coalescence of these latter precipitates. Globally, the beginning of the overageing can be associated to the rapid decrease of mechanical and electrochemical properties of PbCaSn alloys (Bourguignon et al., 2003).
To delay the overageing phenomenon, annealing treatments are usually performed. These treatments are issued from Transformation-Time-Temperature (TTT) diagrams of Pb-Ca-Sn ternary alloys (Hilger et al., 1996). So, a TTT diagram must be established for each alloy composition. Since the common PbCaSn alloys contain numerous impurities such as Ag, Al, Bi, Sb, Sn that stem from secondary lead used for grid manufacturing, the determination of corresponding TTT curves can become a very tiresome work.

Consequently, in order to avoid the building of several TTT diagrams or the using of secondary elements, it is required to set up new manufacturing processes of lead-based materials which inhibit the recrystallization phenomenon. In this context, it becomes pertinent to introduce a secondary phase at the grain boundaries which exhibits the properties listed below:

i. its mechanical properties (*e.g.* hardness) must be much more higher than those of PbCaSn alloys;
ii. its solubility should be negligible in the lead matrix ;
iii. a thermodynamical equilibrium must be reached between this secondary phase and the matrix.

These properties appear to be quite similar to those encountered in the spatial or aeronautics applications areas for which materials are submitted to high temperature ($T > 0.5\ T_m$) for long working time. For example, the fine dispersion of ceramic particles (*e.g.* yttria, zirconia) in platinum matrix leads to the slow down of the recrystallization. As a general rule, this mechanical reinforcement namely called ODS (Oxide Dispersion Strengthening) was widely dedicated to high temperature alloys (Reppich, 2002). Among the benefits effects, the fine dispersion of ceramic particles through the alloy specimen allows anchoring the grain boundaries, prohibiting the discontinuous transformations (*i.e.* recrystallisation or overageing) and standing in the way of the dislocation movement.

Several manufacturing methods of ODS lead-based alloys have been reported in the literature. In particular, previous studies deal with the interest of physical methods. Jiang et al. (Jiang et al., 1998) were able to elaborate nanosized lead powders by using a pulsed wire discharge. This discharge is generated from a thin lead film and leads to its vaporization under the form of fine lead particles. Therefore, no study displays the ability to produce *in situ* composites lead-based powders. Nevertheless, an uncommon work (Devaux et al., 1997) succeeds the elaboration of nanocomposites bismuth-antimony-silica powders thanks to an arc plasma assisted melting method. This latter allows synthesizing fine, pure metallic and ODS powders from a versatile process.

Otherwise, the chemical way has been also investigated to prepare lead-based composite powders (Tilman et al., 1971). So, the Pb-Al_2O_3 composite has been elaborated in high amounts from the precipitation of aqueous solution of $Pb(NO_3)_2$ and $Al(NO_3)_3$,$9H_2O$ in presence of $(NH_4)_2CO_3$ and NH_4OH at controlled value of pH. After washing, drying at 120°C then at 450°C and 600°C, mixtures of alumina and lead monoxide powders have been obtained. Finally, the Pb-Al_2O_3 composite was synthesized by heating the starting mixture under a reducing atmosphere (*i.e.* hydrogen) at 300°C for 18 h. According to these authors, the sintering must be conducted under flowing hydrogen between 300 and 315°C for 24h. Another method has been tried some years earlier by Roberts (Roberts, 1964). This latter consists in mixing a lead powder for 6h at room temperature under air to form thin oxide layer on the grain surface. This layer is crushed and then dispersed within the powder during its shaping by extrusion. Therefore, a recent work (Balaz et al., 2004) reported that the synthesis of lead-based powder during milling of a lead sulphide powder could be considered. In fact, the predominant reaction is the reduction of the lead sulphide in presence of iron issued from the wearing of steel balls:

$$PbS_{(s)} + Fe_{(s)} \rightarrow Pb_{(s)} + FeS_{(s)} \quad (1)$$

The conversion rate can reach 84% after an hour of milling. In these conditions, it can be noticed that the average diameter of particles tends to 15 nm whereas a rising of the milling

time is related to a significant grain growth. For example, the mean grain size could range between 60 and 150 nm for long milling time. Nevertheless, a promising synthesis method has been developed by Dailly (Dailly et al., 2003) and Balan (Balan et al., 2004) for antimony and tin, respectively. This way that relies on the alkaline hydride reduction of metal chloride in the THF solvent provides nanosized metallic particles. These particles appeared to be covered by an alkoxide layer which inhibits both the oxidation and the pre-sintering of powders. Consequently, this method could be easily applied to the elaboration in large amount of ultrafine, pure lead-based powder or lead-lead oxide composite and will be retained afterwards.

The first part of the present chapter is focused on the investigation of the original routes to synthesize lead-ceramic nanocomposites: in particular, the physical route using a plasma arc discharge or the chemical way requiring the reduction of lead-based salts has been selected. In a second part, the potentialities in terms of shaping or sintering of different batches of powders will be examined in comparison with the usual powder metallurgy route (*i.e.* from commercial lead and ceramic powders). In the next section, the mechanical and/or the electrochemical properties of these materials have been determined under the working conditions encountered by lead acid battery grids and have been compared to those obtained for usual PbCaSn alloys. Concerning the electrochemical behaviour, the role played by ceramic films deposited on lead-based substrates has been investigated.

2. Elaboration of lead-based composites

2.1 Synthesis of the pure lead and lead-ceramic powders

The elaboration process differs from the synthesis of the starting pure lead and lead-ceramic composite powders. Before shaping and sintering, the first part of this section will be focused on the description of the different synthesis methods.

2.1.1 Conventional process using commercial powders

This method which is described in details in a previous work (Cartigny et al., 2007) leads to the preparation of lead-ceramic composites which will play the role of "reference" for this study. The lead and ceramic powders (Table 1) were mixed in Turbula apparatus then were

Powder (supplier)	density	Granulometry (μm) furnished by			
		Supplier	Image analysis	Laser granulometry	BET method
Lead (Aldrich)	11.34	40	4.3	-	-
Y_2O_3 (S.E.P.R.)	5.01	<10	1×2 (cubic shaped)	-	0.08
TiO_2 (S.E.P.R.)	4.26	0,2	0.1	0.2	0.09
SiC (Cerac)	3.2	<1	1	-	0.06
SiO_2 (Cerac)	2.2	<5	1	-	0.63

Table 1. Main characteristics of the starting powders

crushed in agate mortar. It must be noticed that ceramic powders such as SiC, SiO_2, TiO_2, Y_2O_3 have been retained because of their chemical inertia in a 5M concentrated sulphuric acid solution. Since the lead grains are partially oxidized as shown by TEM observation and EDXS analysis (Fig.1), the commercial lead powder was previously purified by introducing it in an acid acetic and ethanol mix. Then, the powder was dried under vacuum to remove the solvent traces.

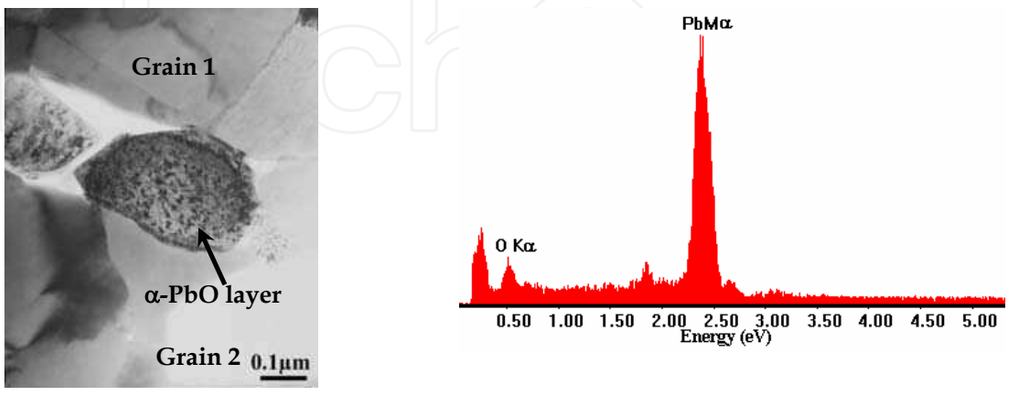

(a) (b)

Fig. 1. TEM micrograph of oxidized lead grains (a) and corresponding analysis of lead oxide by Energy Dispersive X-ray Spectrometry (b)

2.1.2 Synthesis of composite powders assisted by arc plasma process

This method consists in the plasma arc evaporation or co-evaporation of a pure lead anode recovered by silica. This apparatus has been previously described in the literature (Brochin et al., 1999) for the synthesis of bismuth-based composites. The main schema of this device is reported in Fig.2. An electrical arc was produced between a tungsten cathode and an anode-target which is made of the metal to vaporize. For the synthesis of pure lead powder, the molecular hydrogen (H_2) which is dissociated in the arc due to the higher temperature (>10 000K) is dissolved mainly in the metal melt. Its solubility decreases as a function of the distance from the target centre. In the outer part of the metal target, the hydrogen radicals react to form hydrogen molecules. This latter reaction is accompanied by heat emission which enhances the kinetic of the metal vaporization. When a silica target is used to prepare lead-ceramic composite powders, the reaction sequence is quite similar. Nevertheless, further reactions related to silica could occur. First, the silica dissociation leading to the formation of silicon monoxide and molecular oxygen as follows for temperature higher than 3190K:

$$SiO_{2(s)} \rightarrow SiO_{(g)} + \tfrac{1}{2}\, O_{2(g)} \quad (2)$$

Then, the oxygen dissociation occurs when the temperature exceeds 3810K according to equation:

$$\tfrac{1}{2}\, O_{2(g)} \rightarrow 2O_{(g)} \quad (3)$$

Finally, the silicon monoxide transforms into gaseous silicon for temperature higher than 4730K:

$$SiO_{(g)} \rightarrow Si_{(g)} + \tfrac{1}{2}\, O_{2(g)} \quad (4)$$

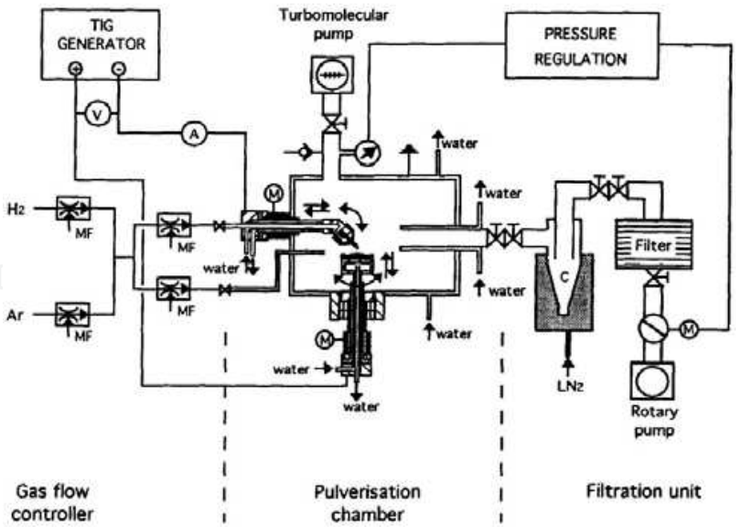

Fig. 2. Device for arc plasma powder production (Brochin et al., 1999)

The first step of the experimental protocol consisted in preparing the metallic anode. So, shavings of lead (99.999%, GoodFellow, UK) which were previously washed in a concentrated acid acetic solution and then in water, ethanol were put in a graphite crucible. The melting of metal was performed under argon (P_{Ar} = 0.13bar) by creating an electrical arc with the cathode. To synthesize a powder of lead-ceramic composite, a silica sheet (99.5%, Heraus, Germany) was put over the metal. A hole was drilled in the centre of the silica sheet to allow the formation of an electrical arc during all the experiment.

The main parameters for the production of pure lead powders have been chosen taking into account the results obtained for the synthesis of bismuth-based powders (Brochin et al., 1999):

i. the working distance between anode and cathode was fixed to 5mm ; the geometry of device coupled with the anode-cathode distance and the residual pressure in the reactor provided the voltage ;
ii. the argon flow ranges between 10 and 12L.min^{-1} to master the powder production. The residual pressure was fixed to 100 torr.

Further experiments have been carried out to find optimised parameters (*i.e.* the anode-cathode distance, the gas flow, the arc intensity) for pure lead powder production. So, for a voltage equal to 16.5V, it appeared that the yield per hour increased when the current intensity was around 60A (Fig.3a). Indeed, a higher intensity inferred a feed powder toward the collector less efficient: some particles agglomerates form a deposit just around the crucible or on the reactor walls. In the same manner, when the current intensity was fixed to 60A, it can be noticed that the yield remains much higher for a voltage near 11-12V (*i.e.* for an anode-cathode distance of 5mm) (see Fig.3b). Finally, under these optimised conditions, a pure lead powder flow of 1g/min can be expected.

In a second step, the synthesis parameters of the nanocomposite Pb-SiO_2 powder have been determined. An argon flow of 10L.min^{-1} has been maintained in the reactor for all the experiments. As revealed in Fig.4a, a good compromise between the yield and the amount of collected powder can be reached for a current intensity of 120A and a voltage initially fixed to 16.5V. In the same way, Fig.4b clearly demonstrates that the voltage between anode and cathode of device should be equal to 16.5V to target the higher powder yield for a

current intensity of 120A. These optimised process parameters have been chosen to obtain a silica content of 2.5 vol.% in nanocomposite powders with a production flow of 3g.min^{-1}.

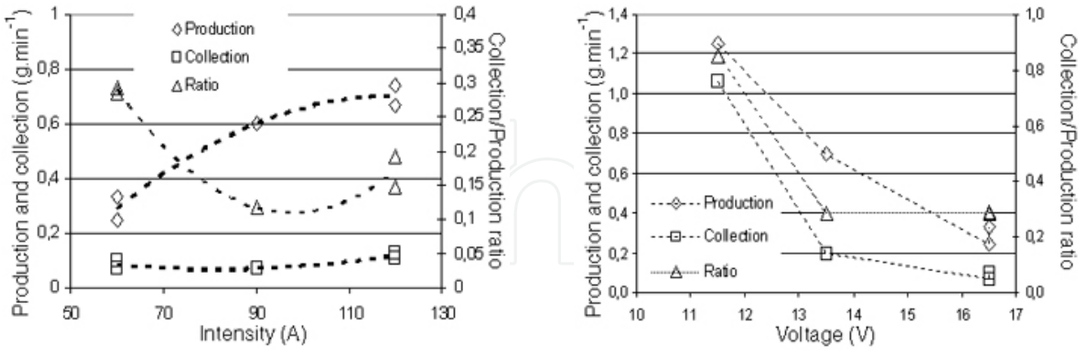

(a) (b)

Fig. 3. Influence on the production, collection and ratio of pure lead powder (a) of electric arc intensity for a given voltage (16V) ; (b) of electric arc voltage for a given intensity (60A)

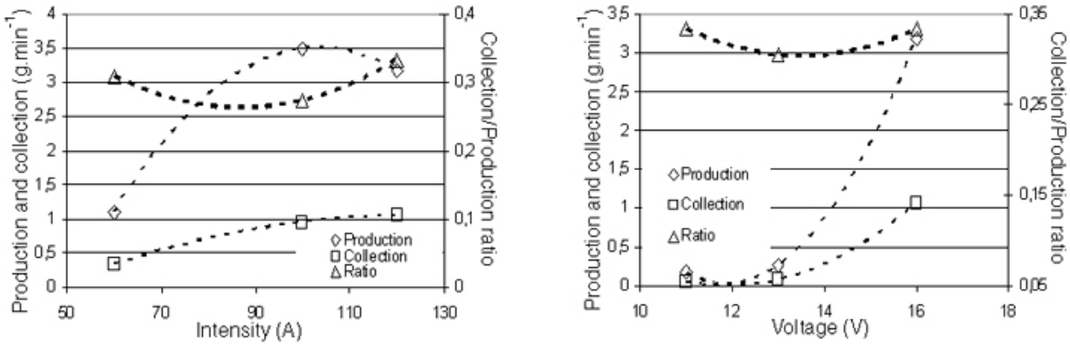

(a) (b)

Fig. 4. Influence on production, collection and ratio of Pb/SiO_2 composite powder (a) of electric arc intensity for a given voltage (16V); (b) of electric arc voltage for a given intensity (120A)

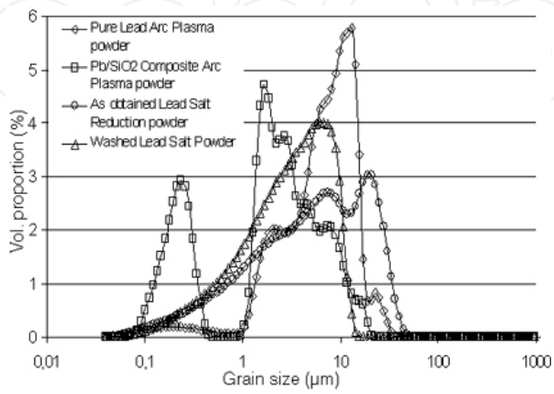

Fig. 5. Grain size distribution for plasma arc powders (pure lead and Pb/SiO_2 composite) and lead salt reduction powders (as obtained and ethanol/water/acetic acid washed)

Pure lead powder synthesized by the plasma arc process does not contain any oxide amount. Nevertheless, this powder is characterized by a wide grain size distribution (Fig.5) which exhibits at least two populations of grains. The first population with an average grain size of around 10µm is associated to the presence of agglomerates which results from the pre-sintering of the elementary particles. Indeed, it can be observed the appearance of necks between particles (Fig.6a) which could be attributed to the early stages of the powder sintering at room temperature. The second population can be associated to a mean grain size of elementary spherical particles (*i.e.* <0.1µm).
In the same manner, the Pb-SiO_2 grain size distribution seems to be bimodal ($\varnothing_{m1}$ = 250nm, $\varnothing_{m2}$ = 2µm) (Fig. 5). The amount of agglomerates which average size is higher than 10µm remains weak. Otherwise, few nanosized particles can be detected from SEM micrographs (Fig.6b). These results are similar to those reported in literature for the synthesis by the same process of Bi-SiO_2 powders (Brochin et al., 1999). Furthermore, the corresponding XRD pattern (Fig. 7) does not reveal silica. That means that the silica phase is not crystallized and/or its contents remains not sufficient to be detected. The appearance of low intensity peaks of the lead monoxide phase can be interpreted considering the characterization conditions (*e.g.* long exposure time in air during XRD experiments).

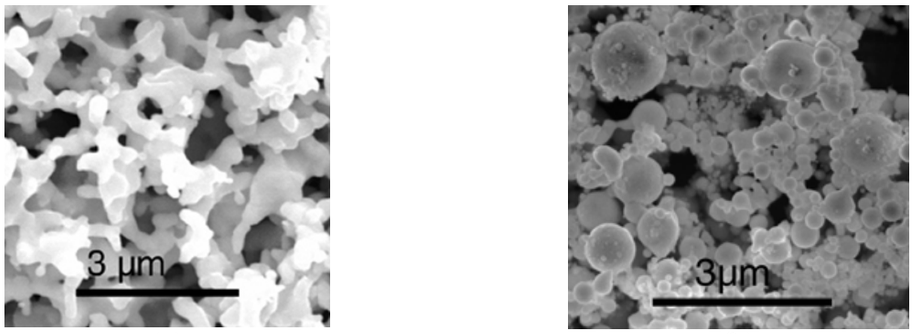

(a) (b)

Fig. 6. SEM micrographs of the plasma arc powders: (a) pure lead, (b) Pb/SiO_2 composite

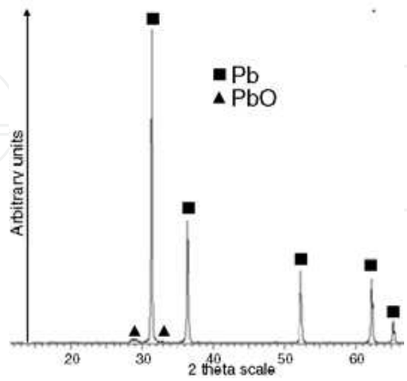

Fig. 7. XRD patterns of Pb-SiO_2 composite obtained by a plasma arc process (JCPDS for lead: 00-004-0686, JCPDS for PbO: 00-035-1483)

The synthesis of pure lead powder by arc plasma process leads to non oxidized powders but with a large grain size distribution for which the higher grain diameter does not exceed few

micrometers. This morphology of so-obtained powders would result from the pre-sintering of pure lead particles at room temperature. Conversely, the elaboration of lead-silica composite powders provides low amounts of agglomerates because of the presence of ceramic particles that inhibits the neck formation between metal particles. The composite powder looks like well dispersed with a bimodal distribution.

2.1.3 Elaboration of composite powders by the route of lead salt reduction

The synthesis of the lead powder rested on the lead salt reduction ($PbBr_2$) by a reducing agent (NaH) according to:

$$PbBr_2 + 2NaH/2tBuONa \rightarrow Pb/2\ tBuONa + H_2 + 2\ NaBr \quad (5)$$

After reaction, the presence de alkoxide in the powder inhibits both the oxidation of lead particles and their agglomeration by pre-sintering (Balan et al., 2004). The stoichiometric proportions of reagents for the reaction (5) were: 2 moles of BuOH (2-methyl-2-propanol, >99%, Aldrich), 4 moles of NaH (55-65%, Fluka) and 1 mole of $PbBr_2$ (>98%, Aldrich). NaH component was beforehand introduced in excess (+5%) so that the reaction (5) can be considered as complete. The quantity of solvent (Tetrahydrofurane (THF)) was equal to 30mL per millimole of lead bromide.

A view of the device used to synthesize the lead powder is proposed in Fig.8. The first step of the experimental protocol consisted in introducing drop by drop the alkoxide (4.4g) in a THF bath (100mL) containing NaH and heated at 100°C. This step was accompanied by the hydrogen release. In a second step, 11g of lead bromide was added to the bath which was then heated at 100°C for 3h. After cooling, the solvent was removed thanks to a rotary evaporator and the powder so obtained was dried under secondary vacuum. Since this powder should be composed (theoretical proportions) of 31.4wt.% Pb, 33.9wt.% NaBr, 31.7wt.% alkoxide, 0.3wt.% NaH, a second washing step in polar solvent was required to remove the residuals salts. Acetonitrile, in spite of its polar momentum (3.92D) was not sufficiently efficient to remove NaBr salt. It was the reason why ethanol (1.62D) has been used first then water (1.85D). In a final step of washing, acetic acid diluted in ethanol to eliminate residual lead oxides has been retained.

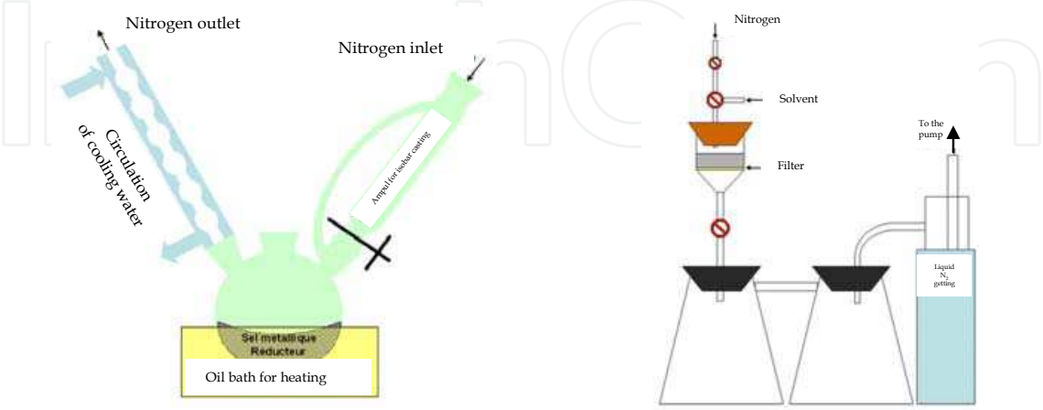

(a) (b)

Fig. 8. Devices for the powder synthesis by lead salt reduction (a) and for washing it (b)

The powders obtained by lead salt reduction and after washing/drying exhibited a small amount of $PbO/PbBr_2$ phases as shown in Fig.9. These observations have been confirmed by TEM characterization of this powder. Indeed, TEM observations (Fig.10a) coupled with electron microdiffraction characterizations (Fig.10b) attested the presence of small oxide particles like plates whereas the lead grains seemed to be spherical with an average grain size of around one hundred micrometers. In particular, the intense diffraction ring detected at 0.299nm could be indexed considering a $PbO\text{-}PbBr_2$ mixed compound (*e.g.* $6PbO\text{-}PbBr_2$) as suggested in the litterature (Knowles, 1951). Otherwise, the grain size distribution spreads out two orders of magnitude between 100nm and 15µm.

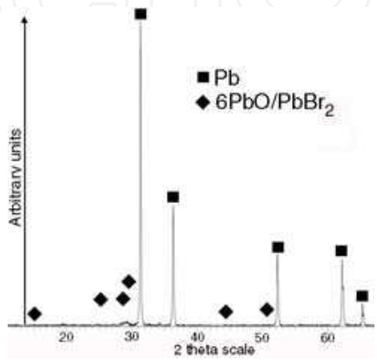

Fig. 9. XRD pattern for an ethanol/water washed powder (JCPDS file for lead: 00-004-0686, JCPDS file for $6PbO/PbBr_2$: 00-006-0384)

(a) (b)

Fig. 10. (a) TEM observation of washed lead salt reduction powder, (b) corresponding electron microdiffraction pattern of the $Pb_xBr_yO_z$ compound

2.2 Thermal behaviour and shaping

2.2.1 Calcination of powders

The thermal behaviour of powders obtained from the physical and chemical routes has been analysed from Differential Scanning Calorimetry (DSC) runs. The DSC thermograms of lead-based powders appear to be different as a function of the synthesis method. So, the thermograms of plasma arc powders only display an endothermic peak which can be associated to the lead melting point (Fig.11a). The corresponding peak shifts toward the lower temperature what would be due to the small particles size of the starting powder (Ben David et al, 1995).

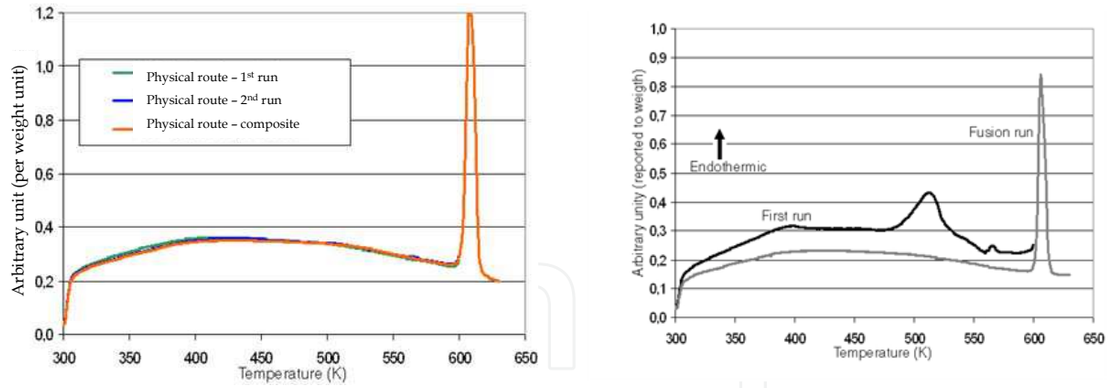

(a) (b)

Fig. 11. DSC thermograms of the lead-SiO_2 plasma arc powder (a) and of the ethanol/water/acetic acid washed lead salt reduction powder (heating rate = 3K.min^{-1}) (b)

The DSC thermogram of the lead salt reduction powder after washing with ethanol, water and acetic acid (Fig.11b) shows a weak endothermic peak near 400K. This thermal effect could be attributed to the vaporization of ethanol or acid acetic traces. Moreover, a second endothermic peak is detected at 480K and is associated to the lead (II) acetate removing. Finally, the displacement toward the lower temperatures of the lead melting peak remains characteristic of the presence of fine lead particles.

2.2.2 Shaping and sintering

Whatever the starting powders, discs of 20mm diameter have been prepared at room temperature by uniaxial pressing with an applied load of 220MPa. Then, the samples have been hot pressed under vacuum (PO_2 < 10^{-6} Pa) thanks to a specific device developed in LCSM laboratory (Cartigny et al., 2007). The choice of the sintering parameters (*e.g.* temperature, soaking time) resulted from dilatometric experiments carried out for commercial pure lead and lead-ceramic mixtures. These parameters have been applied to the whole of compacts obtained from the arc plasma and lead salt reduction powders. As an example, Fig.12 shows dilatometric curves of pure lead and Pb-0.5vol.%TiO_2 compacts which appear similar until 225°C. The average thermal expansion coefficient (α), calculated between 20 and 225°C, was approximately equal to 22.7×10^{-6} K^{-1}. Between 215 and 235°C, a rapid changing of the dilatation rate was observed. For upper temperatures, linear dilatation behaviour can be noticed. Moreover, these observations gave rise to the following comments: i) no shrinkage was observed during thermal treatment, ii) the dilatation effect was more important for pure lead than for composite.

To understand this "anomalous" dilatation for pure lead, several samples were pulled out the dilatometer at 215 and 260°C to be air quenched. After cooling, SEM micrograph allowed to establish the grain size distribution (Fig.13) which showed the dependence between the grain size distribution and temperature. So, for the higher temperature, new particle ranks appeared for the greater diameters, *i.e.* between 12 and 20µm. That could be related to the appearance of an abnormal grain growth mechanism during the thermal treatment. Moreover, Fig.14b confirms the presence of coarse grains ($\varnothing_m$>8µm) only when the pure lead sample is treated at the higher temperatures. The coarse grains are well detected by comparison of heated sample microstructures with those of non-treated samples (Fig.14a). This abnormal grain growth would be probably due to the secondary

recrystallisation process that could occur for the cold-pressed lead samples. Conversely, lead-TiO_2 composite keeps a fine microstructure (Fig.14c) what can be imputed to the presence of fine ceramic particles at the grain boundaries that delays the motion of recrystallisation fronts during heating.

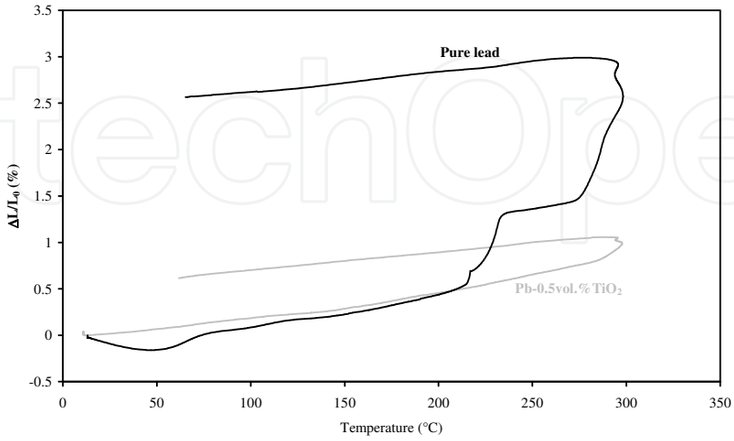

Fig. 12. Shrinkage curves of pure lead and Pb-0.5vol.%TiO_2 compacts

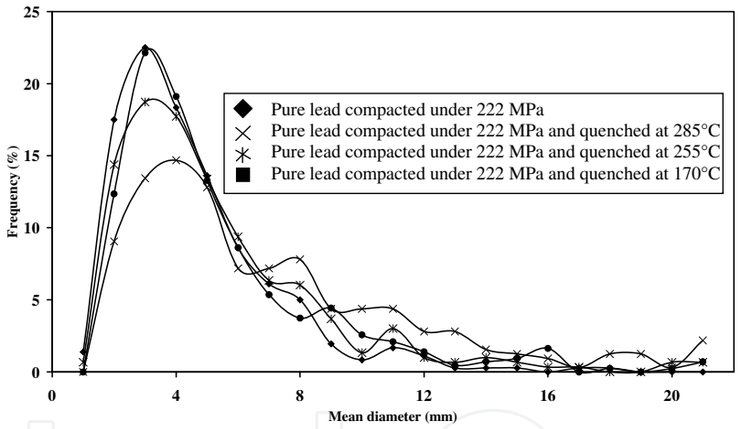

Fig. 13. Grain size distribution for pure lead compact as a function of thermal treatment

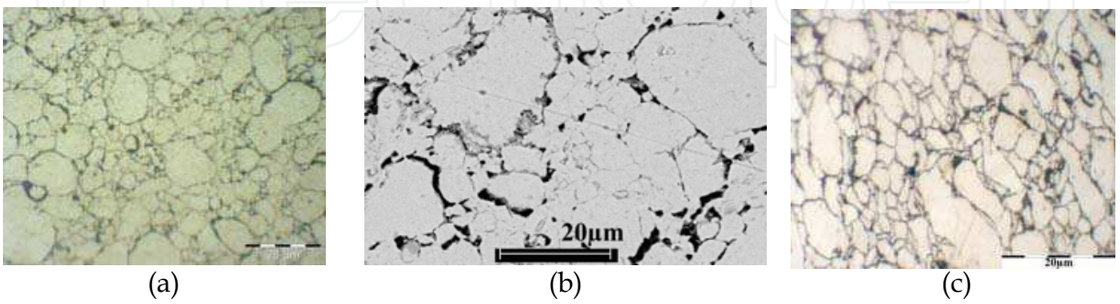

(a) (b) (c)

Fig. 14. Optical micrograph of non treated pure lead sample (a); SEM micrograph of pure lead sample treated until 260°C in the dilatometer (b); optical micrograph of the Pb/(0.5vol.%)TiO_2 composite treated until 260°C in the dilatometer (c)

To improve the densification process, sintering experiments under pressure were carried out for both pure lead and lead-TiO_2 composites. Several thermal and pressure cycling have been tested for pure lead as shown in Fig.15. The densification rate and the average grain size so-determined have been reported for pure lead in Table 2 as a function of experimental conditions. In densification terms, the better results (about 98% of the theoretical value) are obtained by coupling pressure and temperature as indicated in Fig.15b.

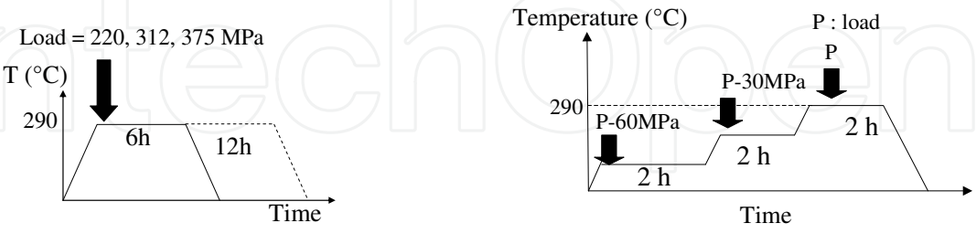

(a) (b)

Fig. 15. Temperature and pressure cycling used for the sintering of pure lead compacts

	Sintering process as described in Fig.15a			Sintering process as described in Fig.15b	
	Load P (MPa) applied during 12 hours			Load P (MPa)	
	220	312	375	220	375
Average grain size (μm)	4.8	5.5	7.7	7.7	8.3
Relative density (ρ/ρ_0)	85.6	98.8	95.0	97.8	97.8
Initial hardness (HV_2)	15.7	10.7	10.4	8.9	9.4

Table 2. Main characteristics of lead samples sintered as mentioned in Fig.15 (with final temperature equal to 290°C)

In a second time, this optimized sintering process has been applied to the lead-ceramic composites. The main characteristics of the sintered samples (relative density, average grain size) have been reported in Table 3 as a function of ceramic used as strengthened agent (SiC, SiO_2, TiO_2 or Y_2O_3). The higher densification rate is reached when titanium dioxide powder is employed. This result can be associated to the good distribution of titanium dioxide particles at the grain boundaries (Fig.16). Moreover, the optimum TiO_2 volume fraction corresponds to 0.5 % because the relative density drops drastically for the higher ratio. This effect is probably due to both the residual porosity in TiO_2 aggregates and the removing of metal-metal junctions for the higher ceramic contents.

Finally, the sintering treatment reported in Fig.15b has been conducted to sinter the plasma arc and lead salt reduction powders. As an example, the relative density of pure lead plasma arc powder reaches up to 99.3% after hot pressing. No shrinkage or dedensification has been detected. In the same manner, the microstructure of hot pressed Pb-SiO_2 composites appears to be characteristic: dense zones (95% of the specimen surface) coexist with porous zones showing macro-cracks (5% of the specimen surface). (Fig.16a). Otherwise, the values of the relative density vary between 93 and 98.5%. From TEM investigations, these variations can be related to the ceramic content: the higher ceramic particle density, the higher residual porosity is. Moreover, silica particles appear to be amorphous, spherical and mainly located at the grain boundaries (Fig.16b).

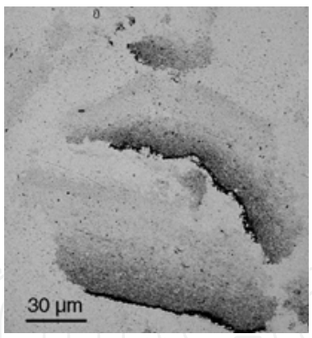

(a)

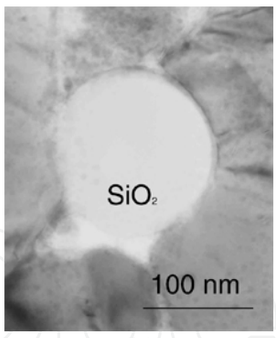

(b)

Fig. 16. Hot compacted plasma arc powder (a) and silica particle at grain boundaries (b)

Nature of material	Volume fraction (%)	Average grain size (µm)	Relative density (ρ/ρ_0) (%)	Hardness (HV_2)	Stationary creep rate (s^{-1})
As-cast pure lead	-	> 300	-	-	$1.40\ 10^{-7}$
Pb-0.08%Ca-2.0%Sn alloy	-	150	-	-	$1.91\ 10^{-8}$
Sintered pure lead	-	7.2	97	-	$2.36\ 10^{-8}$
Pb/TiO_2 (Tioxyde)	0.5	5.6	97.8	13.3	-
	1	5.5	97.7	13.0	-
	3	5.0	96.6	15.1	-
	5	5.9	96.7	16.7	$6.47\ 10^{-10}$
Pb/Y_2O_3 (S.E.P.R.)	0.5	5.9	95.5	12.2	-
	1	5.8	96.7	13.9	-
	3	5.9	97.0	14.8	-
Pb/SiC (Cerac)	0.5	4.5	95.5	13.2	-
	1	4.9	96.3	13.8	-
	3	4.7	96.5	16.0	-
Pb/SiO_2 (Cerac)	0.5	6.2	96.4	10.9	-
	1	7.1	94.3	10.6	-
	3	7.7	93.9	10.4	-
Pure lead (arc plasma route)	-	0.7	99.3	6.0	$9.19\ 10^{-10}$
Pb/SiO_2 (arc plasma route)	2.5	0.25-10	98.5	15.0	$8.00\ 10^{-11}$
Pb/(6PbO-$PbBr_2$) (lead salt reduction route)	-	0.1-10	74	50.0	$4.67\ 10^{-11}$

(*) The creep tests have been performed under a 1.15 MPa pressure at 80°C.

Table 3. Average grain size, relative density, creep rate (*) values for the as-cast pure lead, the as cast and annealed Pb-0.08%Ca-2.0%Sn alloy, the sintered pure lead and the sintered lead-ceramic composites

Before sintering, the microstructure of the lead salt reduction powder compacts is characterized by dense bright and porous dark zones (Fig.17a). On the basis of EDXS analyses, the bright zones (Fig.17b) are only composed of lead whereas the dark zones (Fig.17c) are associated to high content of brome, oxygen and acicular particles. These observations are in a good agreement with those of the starting powder which revealed the presence of lead oxybromide phase giving to this powder a composite character.

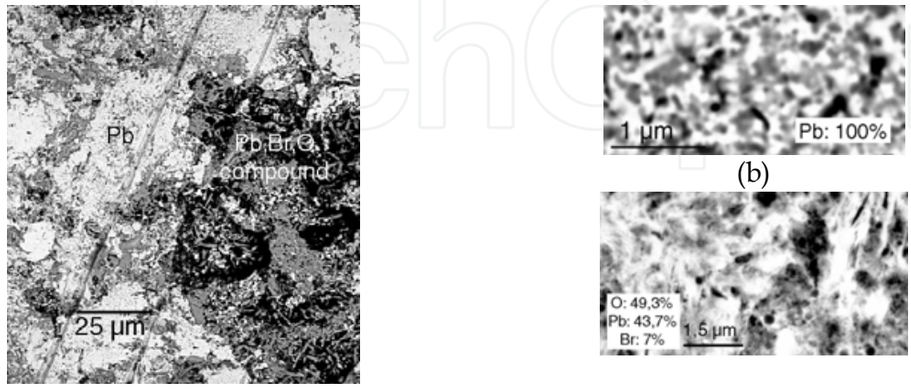

(a) (b) (c)

Fig. 17. SEM morphologies of green lead salt reduction compacted powder (a); SEM observations at higher magnification of the bright zone (b) and of the dark one (c)

Dilatometric tests have been carried out on lead salt reduction powders compacted under a 220MPa applied load. Shrinkage can be observed from 350K (Fig.18) and could be related to both the weigh loss detected on the TGA thermogram (Fig.18) and the endothermic peaks revealed on the corresponding DSC thermogram (Fig.11b). All these effects can result from the vaporization of organic compounds. The relative density value of compacts ranges between 64% and 74% before and after sintering, respectively. It can be noticed that the heat treatment remains similar to that described in details in Fig.15b.

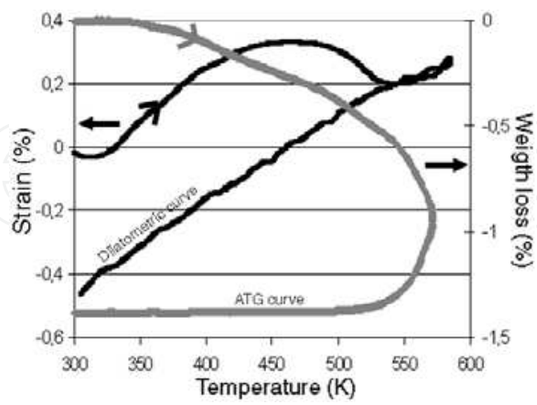

Fig. 18. Shrinkage and TGA curves during sintering of lead salt reduction powder

The microstructure of the sintered material is characterized by the coexistence of two zones which show different sintering behaviour (Fig.19): a full dense lead enriched zone and a porous lead oxybromide zone. In particular, SEM observation confirms the low densification of the $Pb_xO_yBr_z$ zone since this latter makes the propagation of microcraks easier (Fig.19).

Moreover, XRD investigations indicate that the sintering treatment lead to the crystallization of the oxybromide phase with the $6PbO\text{-}PbBr_2$ composition.

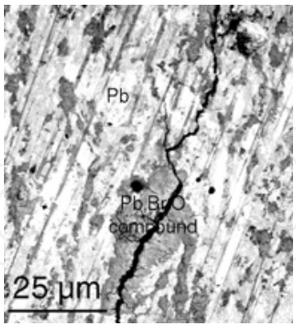

Fig. 19. SEM micrograph of sintered lead salt reduction powder

3. Working properties

3.1 Mechanical properties

3.1.1 Hardness tests

In a first step, the hardness evolution as a function of time at room temperature has been compared between the as-cast lead-based specimens and the lead-ceramic composites (Fig.20). Here, the composites specimens have been prepared from the commercial lead and ceramic powders according to the procedure detailed in section 2.2. In particular, the hardness curve of the as-cast Pb0.08wt.%Ca2.0wt.%Sn alloy then annealed for 2h at 90°C to prohibit the overageing appearance (Maître et al., 2003) has been reported in Fig.20a. This ternary composition is often considered as promising for the development of new acid battery grids (Bourguignon et al., 2003). From Fig.20a, it is well demonstrated that the ceramic addition to pure lead matrix leads to a significant hardness increase as well as its stabilization vs. time. The titanium dioxide addition allows reaching the higher hardness value, *i.e.* 13Hv, confirming the efficiency of the fine particle distribution. Conversely, the hardness of PbCaSn alloy widely fluctuates (Fig.20). These variations can be imputed to both the slow return to its thermodynamic equilibrium state.

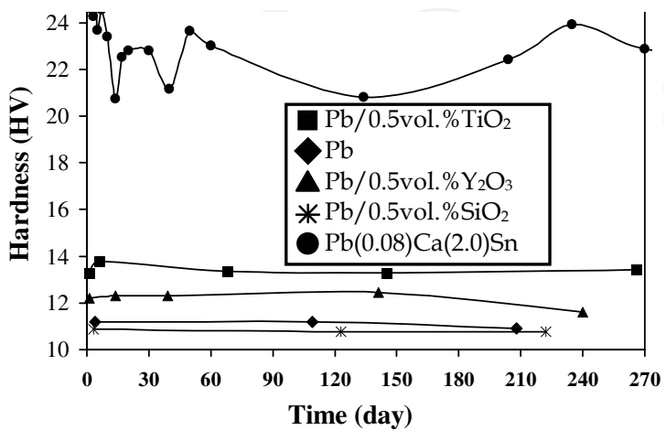

Fig. 20. Hardness evolution at room temperature of sintered pure lead and lead-ceramic composites as a function of time

It can be noticed that the stability of mechanical properties is also encountered for sintered specimens. So, the hardness of the Pb-SiO_2 specimens is about $15Hv_2$ and remains constant for 20 months (Fig.21a). In the similar way, the hot pressed salt lead reduction powder shows hardness values near $50HV_2$. Moreover, this latter is not significantly modified after a heat treatment of 15 days at 80°C or 110°C (Fig.21b).

In summary, although the microstructure of PbCaSn alloy is coarser ($\varnothing_m \approx 100$ µm (Bourguignon, 2003) in comparison with composite materials, its hardness value remains the higher. Consequently, it means that the $L1_2$ phase precipitation and the tin (sub)grain boundary segregation are only responsible of this hardening phenomenon.

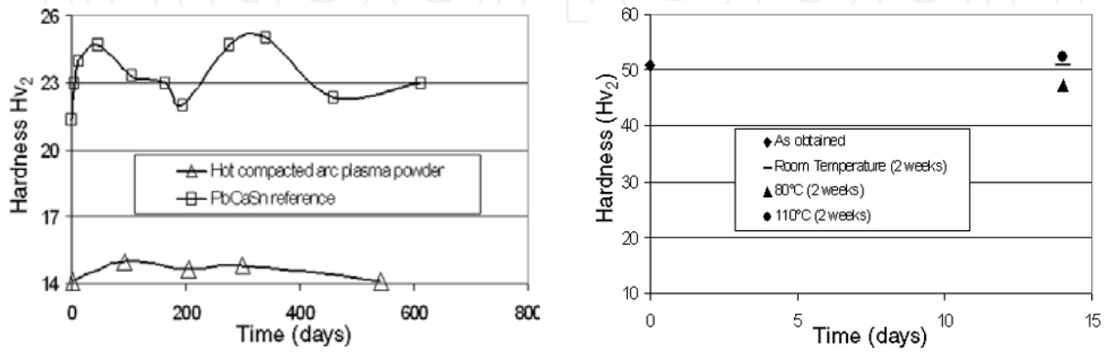

(a) (b)

Fig. 21. Evolution of the hardness value as a function of the ageing time for hot pressed arc plasma Pb-silica (a) powder and hot pressed lead salt reduction powder (b)

3.1.2 Creep resistance

In acid battery applications, the determination of working mechanical properties usually consists in evaluating the grid material creep resistance. Indeed, the positive electrode is chemically corroded during the charge process and the corresponding corrosion product (mainly lead dioxide) has a higher specific volume than the starting material (lead alloy). The tensile stresses on the grid so created during service lead to the growth of the positive plate. Therefore, the positive grid material should have a high creep resistance to prohibit the growth rate in service (Bagshaw, 1995).

The creep resistance of Pb-based materials has been measured thanks to compressive tests with a strain of 1.15MPa. A specific device has been developed in LCSM laboratory and has been previously described in details in literature (Cartigny et al., 2007).

In a first step, the evolution of the strain rate as a function of time under 1.15MPa at 80°C, for as-cast pure lead, annealed Pb0.08Ca2.0Sn alloy, sintered commercial pure lead and sintered Pb-(0.5%vol.)TiO_2 has been reported in Fig.22. For each positive electrode material, the creep rate is calculated in stationary conditions, *i.e.* for secondary creep step from the curves of Fig.22. The data so obtained are reported in Table 3 with the corresponding average grain size of sample. These experiments have been carried out to simulate the curing and the formation steps experienced by each alloy during the battery process (Cooper, 1998).

For as-cast pure lead, the creep rate values are compatible with those mentioned in previous works (Gifkins et al., 1967). Globally, the sintered lead creep rate is close to that of PbCaSn alloy which shows the higher mechanical properties of the as-cast grid alloys. Otherwise, the

creep rate of the Pb-TiO_2 composite (*i.e.* manufactured by mixing commercial powders) appears to be lower of two orders of magnitude than the annealed Pb-Ca-Sn alloys. In the same way, the composites produced from the arc plasma or the lead salt reduction powders show the better creep resistance: indeed, their creep rate varies between 5 and 8.10^{-11} s^{-1} (Table 3). Finally, the grain size of grid material as well as its composition (*i.e.* nature and volume fraction of ceramic) seems to play a major role on the improvement of its creep resistance. In particular, the creep rate of the sintered pure lead drastically decreases when the coarse commercial powder is preferred to the sub-microsized arc plasma powder (Table 3).

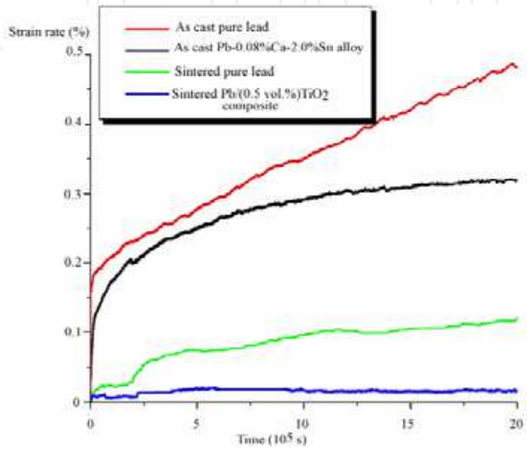

Fig. 22. Creep resistance at 80°C under a 1.15MPa load of as-cast pure lead, as-cast Pb0.08%Ca2.0%Sn alloy, sintered pure lead and sintered Pb-SiO_2 composite

3.2 Corrosion resistance

The overcharge conditions are simulated by a polarisation test at 1.5V for 5 days in 5M sulphuric acid maintained at 20°C. The corresponding curve i=f(t) for the annealed Pb0.08%Ca2.0%Sn alloy is reported in Fig.23a. It can be observed the presence of current variations probably due to the oxygen release. This latter leads to the lead oxide layer micro-cracking and the quasi-simultaneously electrode re-oxidation. Moreover, a low weigh loss is measured after the polarisation test achieved in overcharge conditions (Table 4).

Sample	Weight loss ($mg.cm^{-2}$)
As-cast lead	64.4
Annealed Pb0.08%Ca2.0%Sn	12.5
Sintered lead	166
Sintered Pb-0.5vol.%TiO_2	99

Table 4. Weight loss values measured after polarisation tests in overcharge conditions for as-cast lead, annealed PbCaSn alloy, sintered lead, sintered Pb-(0.5 vol.%)TiO_2

The i=f(t) curve of the sintered Pb-TiO_2 composite (Fig.23b) is characterized by a higher current density in overcharge conditions. This poor corrosion resistance of sintered samples relies on their residual open porosity. Indeed, the electrolyte, *i.e.* sulphuric acid, can preferentially seep in the pores (Figs 24a, 24b) leading to the grain loosening (Fig.24c). In these conditions, the weight loss measured can reach $130mg.cm^{-2}$. This interpretation can be

applied to the corrosion behavior of composites manufactured from arc plasma or lead salt reduction powders since their respective i=f(t) curve (Fig.23c) and their microstructural features after the polarization test remain quite similar.

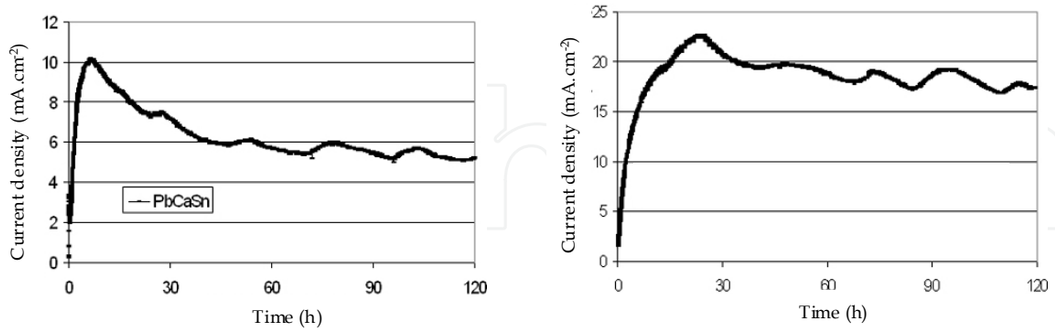

(a) (b)

Fig. 23. i=f(t) curves for annealed PbCaSn alloy (a), sintered Pb(0.5vol.%)TiO_2

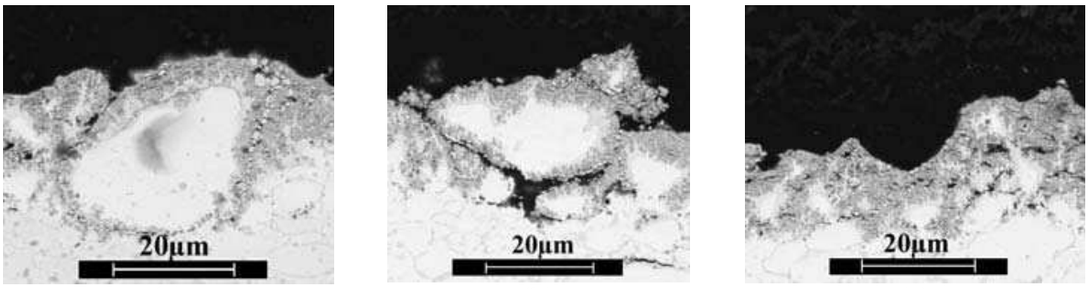

(a) (b) (c)

Fig. 24. SEM cross sections of sintered lead/corrosion products interface after the polarization test of the sintered lead-TiO_2 composite

3.3 Discussion and conclusion

The main properties of lead-based materials are reported in Tables 3 and 4. It clearly appears that the material elaborated from the lead salt reduction powder would present promising mechanical performances. Its hardness is higher than that reported for the other sintered or as-cast lead based materials. Although its densification is not complete, this material keeps the highest creep resistance in comparison with the other composites. Further comments and interpretations are detailed below.

The commercial powders usually lead to working properties depending on both the grain size and the oxide content of starting precursors. The presence of lead monoxide in all the batches allows blocking the grain boundary motion and, consequently, inhibiting the exaggerated grain growth. Otherwise, the lead oxide particles play the role of a strengthening agent within the matrix by displaying strong structural relationships with the lead particles. Consequently, the mechanical properties of composite would be enhanced in comparison with those of the reference (*i.e.* pure lead specimen): for example, the creep rate decreases by 40% and its hardness which remains stable for two years increases by 1.5 Hv_2. Nevertheless, the features of the commercial powders can deeply differ from one batch to another requiring the determination of the sintering parameters once again.

The compacts manufactured from pure lead arc plasma powder obviously show similar mechanical properties than those of the as-cast pure lead specimens. This result could be explained by considering the evolution of the grain boundary concentration throughout the elaboration process. Indeed, the pure lead powder appears to be partially sintered just after synthesis then the sintering treatment promotes the grain growth of the coarser lead particles. To explain their similar mechanical behaviour, one must consider that the grain boundary density is finally near between the two types of pure lead specimens.

The sintered bodies issued from Pb-SiO_2 and Pb-(6PbO-$PbBr_2$) are characterized by promising mechanical properties (Table 3). This observation results from the dual-acting of the homogeneous dispersion of hardening particles within the lead powder and the optimum content of non metallic grains. These conditions would be then fulfilled by using the arc plasma or the lead salt reduction process as synthesis method of composite powders. Nevertheless, some efforts should be done to obtain full dense materials by determining the adequate parameters of the sintering treatment. Actually, the presence of residual porosity for the current sintered Pb-(6PbO-$PbBr_2$) composite is probably the cause of the weakness of the creep resistance. Nevertheless, the weak corrosion resistance of this latter composite could limit its implementation as electrode materials in battery. Indeed, it is well known that the positive electrode in an acid battery reaches periodically voltage values ranging between 1.3 and 2.1V. This phenomenon is accompanied by the periodical conversion of dibrome (Br_2) to bromide (Br^-) according to the Pourbaix diagram. At this stage, it must be noticed that the dibrome specie could be liquid at the acid battery working temperature what could review the ability to use this composite as electrode.

Finally, the using of sintered composite materials are not affected by the appearance of softening structural transformations such as recrystallisation or overageing since these systems have reached their thermodynamical equilibrium. As a result, their microstructures as well as their mechanical properties remain stable as a function of time. Conversely, variations by 25% are usually registered for the hardness value of a Pb0.08%Ca2.0%Sn alloy. Otherwise, it appears that the weakness of the sintered materials comes from their electrolytic permeability which depends on their residual porosity. To avoid this phenomenon, the deposition on the composite system of thin coating could fill the residual open porosity without decreasing their mechanical properties.

4. Protective coatings against the corrosion

In a first step, the using of electrolytic coatings of pure lead or lead-tin alloy represents a promising method to promote the corrosion resistance of sintered composite in concentrated sulphuric acid. Indeed, these coatings allow both protecting the surface and keeping the high mechanical properties of the sintered substrate.

In a second step, the improvement of the corrosion resistance can be reached by implementing a coating process of active elements. Indeed, the lifetime of positive electrodes is related to the active matter decohesion which leads to the loss of electron conductivity and battery electrical capacity. So, the role of the active elements on the adhesion of oxide layers would claim to be explored. Previous studies (Bourguignon, 2003) have shown that the presence of a mixed oxide phase at the alloy-corrosion layer could improve the corrosion resistance of the lead-based alloy in the concentrated sulphuric acid.

This section is then focused on the implementation of lead-based coatings and of silica-based thin layers. To understand well the role of ceramic coatings on the electrochemical

corrosion of electrode materials, coatings have been deposited on reference-like substrates of PbCaSn alloys for which the corrosion process in H_2SO_4 is well known.

4.1 Lead-based coatings

4.1.1 Experimental procedure

Before coating, the substrates were polished, washed, dried and weighted. The cleaning resulted from the using of trichloroethylene as a solvent for 30s then the washing with water. The pickling was conducted with either the HBF_4 (8%)/H_2O_2 or acetic acid/H_2O_2 mixtures for 30s before a cleaning with HBF_4 to avoid the contamination of electrolytic bath. The electrolytic bath is a solution of HBF_4 containing 130g.L^{-1} of lead (Jobst *et al.*, 1997). The preparation of this bath is described in a previous study (Subramanian *et al.*, 1966). According to the literature, the current density was chosen ranging between 1 and 8A.dm^{-2}

4.1.2 Influence of the current density

Low current density values (*i.e.* between 2 and 3A.dm^{-2}) provide a homogeneous lead layer on a substrate manufactured by sintering of as-treated commercial lead powder (Fig.25a). The thickness of this layer so-obtained is about of 60µm. To improve the adhesion of this coating on lead-based substrate, an annealing treatment for 6h at 80°C has been performed. Nevertheless, the residual stresses probably due to the hydrogen insertion in the coating lead to its desquamation (Fig.25b). To solve this problem, it was decided to decrease the current density up to 1A.dm^{-2} during deposing process to inhibit the residual stresses.

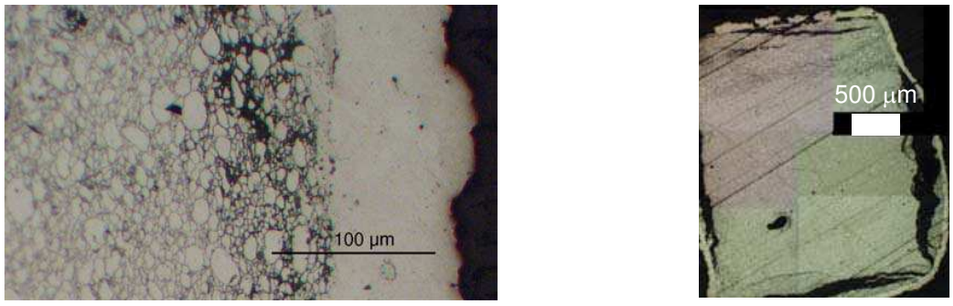

(a) (b)

Fig. 25. Cross sections of the lead electrolytic coatings obtained with a current density of 3A.dm^{-2} (a) and after an annealing of 6h at 80°C (b)

4.1.3 Influence of the annealing temperature

A current density of 1A.dm^{-2} was then employed to elaborate new lead-based coatings. A first annealing treatment which was performed at 80°C seems not to modify the microstructural features of the coating. Since the results obtained for this latter under simulating overcharge conditions were not convincing, further experiments were carried out for higher annealing temperatures. For example, an annealing treatment has been conducted at 110°C under vacuum. This treatment leads to both the decrease of the residual porosity in the substrate and prohibit the breakdown of the coating or substrate.

The cyclic corrosion test is the most representative because it tends to the working conditions of the lead acid battery. So, the potential varies between the battery overcharge 1.5V SHE^{-1} (Hg/$HgSO_4$ electrode) and the battery discharge 0.7V SHE^{-1} during 5 days at

room temperature. In these conditions, the lead-based coating, annealed at 80°C, would be characterized by a drastic increase of the current density after the third cycle (Fig.26). Finally, the current density determined after the corrosion test is two times higher than that of the reference PbCaSn alloy. On the other hand, the corrosion behaviour of the covered specimen, annealed at 110°C, appears to be very different. Indeed, the current density is two times lower than that of the reference. These results are in a good agreement with the measurement of weight losses (*Table 5*) after corrosion.

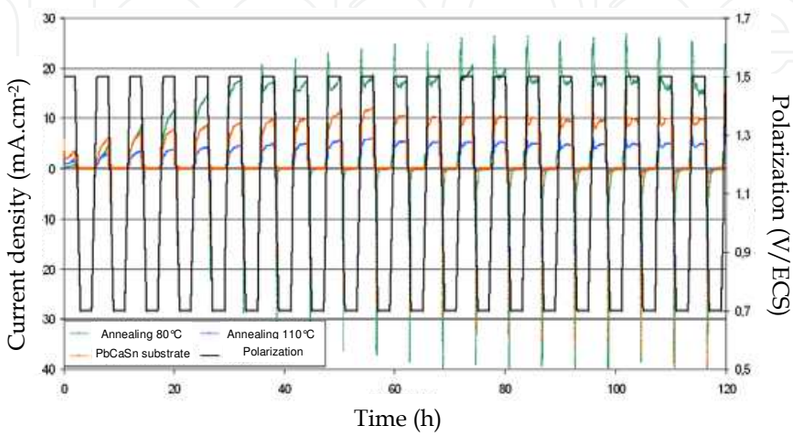

Fig. 26. Evolution of the current density in cyclic conditions for annealed lead coatings

Type of coating	Weight loss (mg.cm-2)
Reference (Pb0.08%Ca2.0%Sn)	20.8
Coated specimens treated at 80°C	147.2
Coated specimens treated at 110°C	16.8

Table 5. Weight loss values measured after corrosion tests for coated, annealed specimens

In particular, the weight loss remains significant for the coating annealed at 80°C which can be associated to the presence of a dense duplex layer. The outer layer would be composed of lead monoxide whereas the inner part corresponds to the lead sulphate compound. This sequence seems to be abnormal with regards to that obtained for the PbCaSn alloy (reference). Moreover, the lead oxide layer is characterized by the presence of lead particle. All these morphological characteristics show that the coating would not be adherent to the substrate. Indeed, the infiltration of electrolyte within the coating could promote the local fluctuation of pH and, more particular, the medium acidification. This latter would prohibit the lead monoxide formation but in the same time would favour the appearance the lead sulphate from the following reaction:

$$Pb + 2H^+ + SO_4^{2-} = PbSO_4^- + H_{2(g)} \quad (6)$$

This phenomenon could come from the residual porosity of the lead coating annealed at 80°C. Conversely, the lead coating treated at 110°C displays an uniform corrosion layer which can be related to the higher density and adhesion of the corrosion products (Fig.27a). The stacking sequence of the corrosion layers is in a good agreement with that observed in previous studies (Bourguignon et al., 2003): an internal thin and continuous layer of lead

monoxide surmounted by coarse $PbO_2\alpha$ and $PbSO_4$ grains. Few residues of corrosion products can be detected under the coating nevertheless, these forays do not cross the lead coatings (Fig.27b).

(a) (b)

Fig. 27. Cross sections after cyclic corrosion test (1A.dm^{-2}) of the lead coating annealed at 80°C (a), at 110°C (b) (local infiltrations of corrosion products under the coating)

4.2 Silica-based coatings

A thin silica layer has been elaborated to improve the anchorage of the active matter during the corrosion of grids.

4.2.1 Experimental protocol

The substrates (15×15×1mm^3) were made of the reference PbCaSn alloy, were previously polished thanks to the using of SiC papers (grade 1200) and then were stored under argon. The Plasma Enhanced Chemical Vapor Deposition (PECVD) method was applied to elaborate thin silica layers. These experiments have been conducted in the SPCTS laboratory in Limoges (France). This way rests on the using of the silane (SiH_4) as silicon precursor. The first coatings have been synthesized by undertaking the pre-treatment of the substrate surface. This latter consists in the polarization at 150V under an argon/hydrogen flow for 15 minutes in order to clean the substrate surface. The microwave power is then fixed to 1000W. In a second step (*i.e.* the deposition step), the silane and the oxygen flows have been chosen as being equal 1sccm and 360sccm, respectively (P_T = 9Pa). The thickness of silica layer so-obtained can range between 80 and 200nm. Further coatings have been prepared without pre-treatment to form 100-1000nm thick layers (Régnier *et al.*, 1996).

4.2.2 Morphological characterization of the coatings

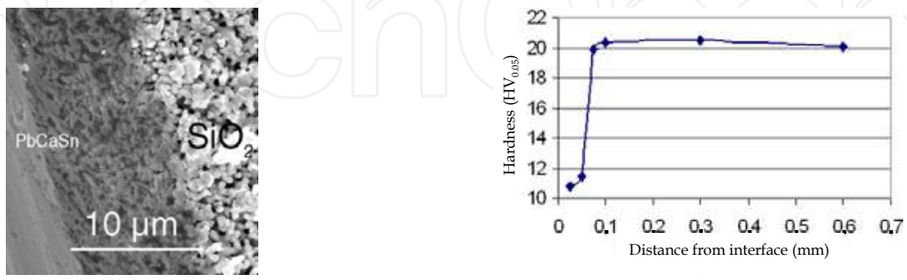

(a) (b)

Fig. 28. SEM micrograph of a breakage of a silica coated specimen (a) ; evolution of the hardness for a silica coated specimen after pre-treatment (b)

The coating of the pre-treated specimens appears to be porous and composed of not agglomerated spherical silica particles. The pre-treatment seems to modify the

microstructure of substrate. In particular, a melted zone can be detected at the silica coating-PbCaSn substrate interface (Fig. 28a). The disappearance of the cast and annealed microstructure of ternary alloys has been confirmed from hardness measurements: the zone submitted to the hydrogen ions beam can be associated to a hardness drastic decrease (Fig.28b).
Conversely, the untreated specimens are characterized by a covering silica layer. No melted zone has been detected from SEM observations or mechanical tests.

4.2.3 Electrochemical behaviour

In a first approach, the electrochemical behaviour of the silica coatings on the PbCaSn substrate has been evaluated from dynamical polarization tests between the free potential and a potential equal to +2V SHE^{-1} ($Hg/HgSO_4$ electrode). The corresponding voltamperogram (Fig.29) clearly evidences the significant effect of the ceramic coating. It cannot be observed for the silica coated specimens the different peaks corresponding to the lead oxidation at -0.9V ($Pb \rightarrow PbSO_4$,PbO) and at 1.45V ($Pb^{II} \rightarrow PbO_2$) (Bourguignon, 2003). Moreover, the peak of solvent oxidation leading to the oxygen release is shifted toward the higher potential value. From these results, it can be expected that the corrosion behaviour under overcharge conditions (1.5V SHE^{-1}) of the covered specimens should be improved by decreasing the released oxygen content and, consequently, by reducing the overall current and the damaging mechanical effect of the gaseous oxygen emission on the corrosion layers.

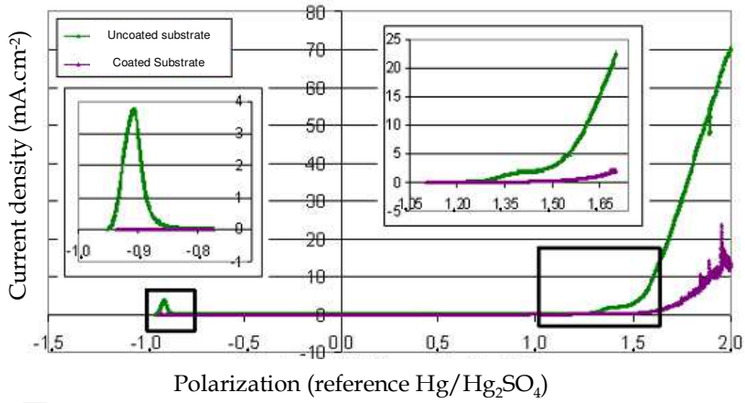

Fig. 29. Voltamperometry curves from the free potential up +2V SHE^{-1} for the uncoated substrate and the coated one

The cyclic voltamperometry curves obtained for potential ranging between -1.8 and 2V show that the silica coatings drastically inhibit the substrate corrosion during the first cycles. Then, several potential scans damage the silica layer and, finally, lead to the electrochemical response of the uncoated substrate. In particular, when the number of cycles exceeds three, the substrate oxidation becomes more sensitive and the $Pb^{+II} \rightarrow Pb^{+IV}$ transformation is clearly visible in the corresponding voltamperograms. In a same manner, the oxidation of the solvent is definitively located at anodic potential values lower than 1.4V.

4.2.4 Corrosion behaviour in the overcharge conditions

The pre-treated and coated specimens present a high current density after 24h at 1.5V in concentrated sulphuric acid (5M) (Fig.30a). The corresponding i=f(t) curve show variations which could be imputed to the oxygen release leading to the lead oxide layer micro-cracking

and quasi-simultaneously electrode re-oxidation. This corrosion behaviour appears to be similar to that observed for sintered specimens even if in the present case the current density value remains lower. Therefore, in the early stages of the corrosion test, it can be noticed that the density current decreases as a function of the layer thickness. Finally, the weight losses are near whatever the pre-treated specimen.

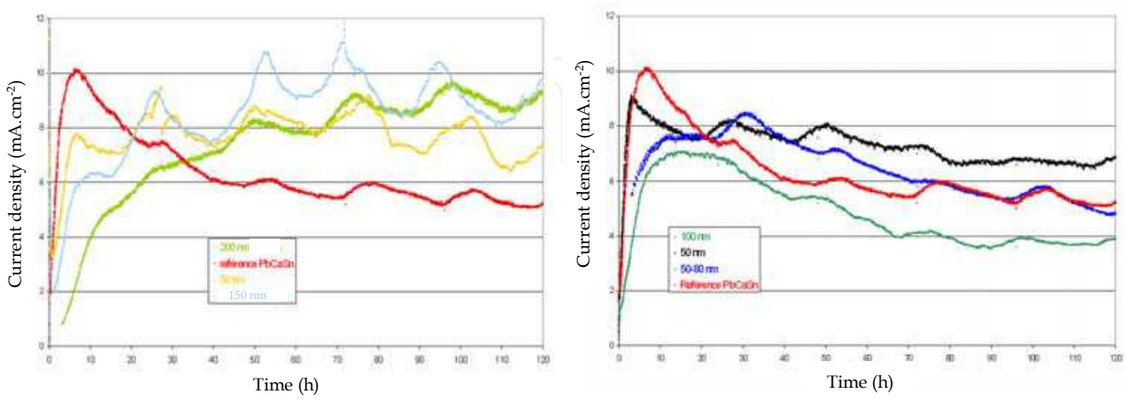

(a) (b)

Fig. 30. Current density in overcharge conditions for pre-treated and coated substrates (a); current density in overcharge conditions for untreated and coated substrates (b)

The benefit of silica coating on the electrochemical behaviour of untreated samples is demonstrated by the significant decrease of the current density after 24h of treatment (Fig.30b). The current corrosion would seem to be correlated to the silica layer thickness. Except for the thicker layer, all the coated substrates tend to keep the same corrosion resistance after one day as revealed by the comparison of the final weight losses. Otherwise, the sequences of corrosion layers remain similar between the coated and uncoated substrates: an inner dense corrosion layer and an outer porous part (Fig.31a). The thickness of the corrosion layer is significantly lower for coated specimens. The observation of SEM cross sections for corroded samples reveals that the corrosion phenomenon occurs along the grain boundaries of PbCaSn substrate (Fig. 31b). Chemical analyses by EPMA show that the silicon is only detected at the substrate/corrosion layer interface. Moreover, no silicate phase like $PbSiO_3$ is observed at this interface.

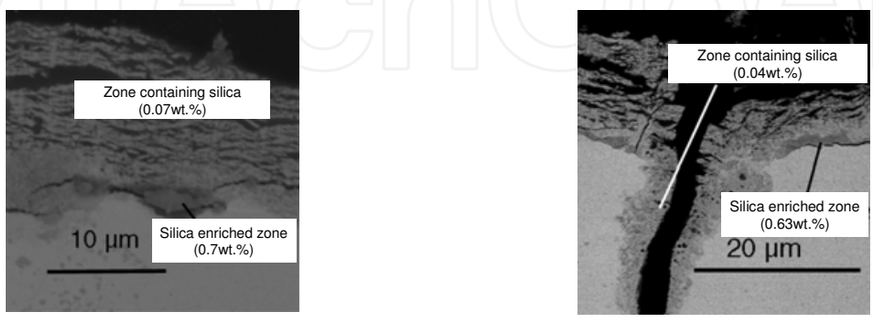

(a) (b)

Fig. 31. SEM observations of cross sections of silica coated specimens after corrosion test in overcharge conditions

4.2.5 Corrosion behaviour in cyclic conditions

The comparison of the current density evolution for different coating thicknesses shows up the slowing down effect of the silica layer on the corrosion kinetics. This positive influence is only significant at first (Fig.32). As soon as the third cycle is reached, the efficiency of the thicker coating (equal to 1000nm) is insufficient to soften the corrosion attack. Conversely, the silica coating for which the thickness is close to 300nm displays promising corrosion behaviour. The morphological features of corrosion layers are similar to those observed in overcharge conditions. The silicon element can be detected either at the corrosion layer/substrate interface or near the outer part of the corrosion layer. These results suggest that no specific corrosion mechanism is encountered for coated specimen but it occurs preferentially in zones where the silica layer is not covering or breakable.

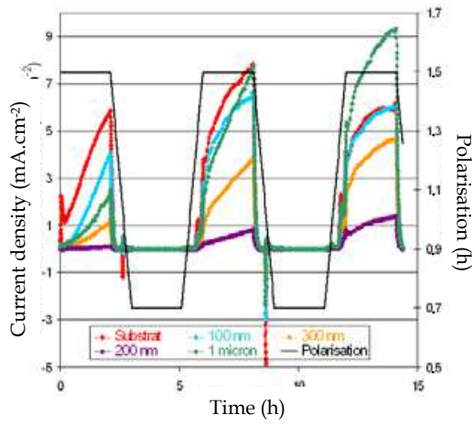

Fig. 32. Evolution of the current density as a function of time in cyclic conditions

4.3 Discussion and conclusion

The lead electrolytic coatings on sintered substrate have been elaborated by using a current lower than that reported in the literature. Indeed, the higher current leads to damaging effects because of the hydrogen trapping in the substrate pores. Hydrogen results from the reduction of proton of the acid electrolyte. An annealing treatment is required to guarantee the substrate protection against the corrosion. The annealing treatment seems to be more efficient at 110°C than at 80°C. Indeed, the increase of the annealing temperature leads to the decrease of both the current density and the weight loss after corrosion test. These promising results have been confirmed by the observations of the corrosion products: the morphology of corrosion layers remains similar to that obtained for polarization achieved at low potential (+0.7V). Concerning the silica coatings issued from PECVD experiments, it is necessary to analyse the specific effect of the "ionic cleaning". The pre-treated specimens usually show non covering silica layer on modified substrate. Indeed, it infers the softening of the PbCaSn substrate by surface melting. This effect is well characterized by the decreasing of mechanical properties (*e.g.* hardness) for pre-treated samples in comparison with those of cast and annealed PbCaSn substrates. These observations allow explaining the weak corrosion resistance of pre-treated samples and are in a good agreement with previous studies (Albert et al., 1997) which mentioned that the volume of released oxygen and the weight loss are more important for non aged alloy. Otherwise, the untreated specimens are characterized by the presence of covering silica layers whereas the substrate appears not to

be affected by the deposition process. The free potential in sulphuric acid is not modified but the current corrosion drastically decreases. In the same manner, the water oxidation moves toward the higher potential values and the lead oxidation ($Pb^{+II} \rightarrow Pb^{+IV}$) is not detected. This behaviour explains the decrease of the current corrosion density that can be observed for the silica coated samples (thickness layer < 300nm) in the early stages of the overcharge test. In this case, the corrosion layer is denser and is composed of silicon-doped phases at the corrosion layer-substrate interface. It can be noticed that the weight losses remain less important for silica coated samples. Thicker silica coatings (e>1μm) have undergone a reversal effect: PECVD technique does not provide adherent silica coatings.
From these results, the doping effect of silicon must be retained to explain the growth of a covering layer of PbO_{1+x} for which the predominant defect is the interstitial anion. This effect is identical to that mentioned in the literature (Bourguignon et al., 2003) concerning the formation of lead monoxide (in overcharge conditions) on the surface of cerium or lanthanum-doped PbCaSn alloys. The equilibrium of the defect formation can be written:

$$SiO_2 = Si^{\bullet\bullet} + O_O + O_i'' \quad (7)$$

It shows that the introduction in the lead oxide lattice of cation belonging an oxidation degree higher than that of lead such as Si^{4+}, La^{3+} or Ce^{4+} leads to enhance the content of predominant defects and promote the growth rate of oxide. Therefore, it can be noticed that a dense corrosion layer is detected just above silica-enriched zones (see Fig. 31a) and Fig. 31b). That means the silicon element could improve the anchorage of corrosion layer on lead-based substrate by forming mixed phases.

5. Conclusion

Three routes for the synthesis of lead-based powders have been investigated. The using of commercial powders which are previously treated in acetic acid bath provides after sintering compacts with a relative density higher than 97% and hardness near 12.5 Hv_2. These performances are linked to the presence of residual oxide and of a wide grain size distribution. Otherwise, the lead powder elaborated by arc plasma method seems to be characterized by agglomeration and pre-sintering effect at low temperature. Consequently, the mechanical properties of pure-lead sintered compacts remain similar to those encountered for as-cast pure lead specimens. Conversely, the arc plasma method provides nanosized, spherical and non agglomerated of Pb-SiO_2 powders. After sintering, the presence of silica intergranular inclusions leads to the mechanical reinforcement of lead-based matrix: in particular, the hardness value reaches 15 Hv_2 and the creep rate is decreased by two orders of magnitude in comparison with the behaviour of the PbCaSn alloy. The third synthesis route consists in reducing lead salts in organic medium. This route gives better mechanical properties for sintered specimens. The powder so-obtained is composed of not well crystallized phases containing brome, oxygen and lead elements. After hot compaction, these oxybromide phases confers promising properties to the lead matrix: a low relative density (74%), a high hardness (>50Hv_2) and a creep resistance that has multiplied fourfold in comparison with that of commercial lead powders. The decrease of creep rate is probably limited by the presence of cracks due to both the solvent removing and the expansion coefficient mismatch between the matrix and reinforcing agent.
Nevertheless, all these sintered materials show a residual porosity and a high grain boundary density. The corrosion tests in overcharge conditions have demonstrated that

these microstructural features are damaging for the electrochemical resistance of lead-based materials. Due to this assessment, a new route has been devised consisting in coating the sintered lead-base substrate with an electrolytic layer of lead. When higher current density values are targeted, it can be observed the mechanical deterioration of the substrate. This phenomenon could be attributed to the stresses correlated to the hydrogen release. So, the electrolytic coatings have required annealing treatments to reach homogeneous and free stress substrates. The electrochemical behaviour appears to be improved for lead-based substrate annealed at 110°C.

The corrosion resistance in concentrated sulphuric acid can be enhanced by putting a thin silica coating on the substrate. This coating could produce mixed oxide layers with the corrosion products making corrosion layers better anchored on the substrate. The silica coating has been elaborated by PECVD. When no pre-treatment is conducted, the substrate microstructure remains unchanged and keeps the aged state. The silica is then covering with a thickness ranging between 100nm and 1μm. The thicker silica layers seem to be subjected to a preferential detachment. Conversely, the silica layers which belongs a thickness varying from 100 to 300nm, a silica-enriched phase is located at the corrosion layer-substrate interface after overcharge conditions. This phenomenon leads to the decrease of the corrosion current during the electrochemical test. These positive trends could be coupled by manufacturing a new lead-based composite allowing to substitute the actual alloys. So, this composite could be composed of a substrate elaborated by hot compaction of lead-based powders synthesized from the reduction lead salts route. This sintered substrate should be covered by a silica layer obtained by PECVD. Such composite should have the mechanical properties of the substrate and electrochemical resistance of the coating.

6. References

Albert L., Chabrol A., Torcheux L., Steyer Ph., Hilger J.P., Improved lead alloys for lead/acid positive grids in electric-vehicle applications. *J. Power Sources*, 67, (1997) pp.257-265.

Bagshaw, N.E., Lead alloys: past, present and future. *J. Power Sources*, 53, (1995) pp.25-30.

Balan L., Schneider R., Billaud Denis, Fort Y., Ghanbaja J., A new synthesis of ultrafine nanometre-sized bismuth particles, *Nanotechnology*, 15 (2004) pp.940–944.

Balaz P., Godocikova E., Takacs, L., Skorvanek, I., Choi, W.S., Kim, B.S, Preparation of nanocrystalline metals by mechanochemical reaction of sulphides with reducing element. *Proc. of the Korea-Japan Int. Symposium on Powder Science and Technology*, pp.237-241, Busan, Korea, November 2005, 2005, Busan.

Ben David T., Lereah Y., Deutscher G., Kofman, R. Cheyssac P., Solid-liquid transition in ultra-fine lead particles. *Phil. Mag. A*, 71 (1995) pp.1135-1143.

Bouirden L., Hilger J.P., Hertz J., Discontinuous and continuous hardening processes in calcium and calcium—tin micro-alloyed lead: influence of 'secondary-lead' impurities. *J. Power Sources*, 33 (1991) pp.27-50.

Bourguignon G., Maître A., Rocca E., Steinmetz J., Torcheux L. Electrochemical study in sulphuric acid of the hardening $L1_2$ phases of Pb–Ca–Sn alloys. *J. Power Sources*, 113 (2003) pp.301-307.

Brochin F., Devaux X., Ghanbaja J., Scherrer H., Study of BiSb-SiO_2 nanocomposite powders produced by an arc plasma processing. *NanoStructured Materials*, 11(1999) pp. 1-8.

Bui, N., Mattesco P., Simon P., Steinmetz J., Rocca E., The tin effect in lead-calcium alloys. *J. Power Sources*, 67 (1997) pp.61-67.

Cartigny Y., Fiorani J.M., Maître A., Vilasi M., Pb-based composites materials for grids of acid battery. *Materials Chemistry and Physics*, 103 (2007) pp.270-277.

Cooper A., The Brite–EuRam lead-acid electric-vehicle battery project—progress report. *J. Power Sources*, 73 (1998) pp.127-145.

Dailly A., Schneider, R., Billaud D., Fort Y., Ghanbaja J. Nanometric antimony powder synthesis by activated alkaline hydride reduction of antimony pentachloride, *J. Nanoparticle research,* 5 (2003) pp.389-393.

Devaux X., Brochin F., Dauscher A., Lenoir B., Martin-Lopez R., Scherrer H., Scherrer S., Production of ultrafine powders of Bi-Sb solid solution. *NanoStructured Materials*, 8 (1997) pp.137-147.

Giess, H.. The influence of calcium, tin and grid thickness on corrosion induced grid growth. *J. Power Sources,* 53, (1995) pp.31-43.

Gifkins R.C., Snowden, K.U., Stress sensitivity of creep of lead at low stresses. *Trans. AIME*, 239 (1967) pp.910-915.

Hilger J.-P., Bouirden L., New representation of the hardening processes of lead alloys by transformation-time-temperature (TTT) diagrams. *J. Alloys and Compounds*, 236 (1996), pp.224-228.

Jiang W., Yatsui K., Pulsed wire discharge for nanosize powder synthesis. *IEEE Transactions on Plasma Science*, 26 (1998) pp.1498-1501.

Jobst, A. Grahl, W. Gruner, Warlimont H. Hardening and Smoothing effects of Lignin Sulfonates on the Electrodepostion of Lead. *J. Applied Electrochemistry*, 27 (1997) pp.455-461.

Knowles L.M., Thermal analysis of the system PbBr2-PbO, *J. Chem. Phys.*, 19 (1951) pp.1128-1130.

Maître, A., Bourguignon G., Fiorani J.-M., Ghanbaja J., Steinmetz J. Precipitation hardening in Pb–0.08wt.%Ca–x%Sn alloys—the role of the pre-ageing. *Materials Science and Engineering A*, 358 (2003) pp.233-242.

Miraglio L., Albert L., Ghachcham A. El., Steinmetz J., Hilger J.P., Passivation and corrosion phenomena on lead-calcium-tin alloys of lead/acid battery positive electrodes. *J. Power Sources*, 53 (1995) pp.53-61.

Reppich B., On the dispersion strenthening mechanisms in ODS materials, *Zeitschrift für Metallkunde*, 93 (2002) p.7.

Régnier C., Tristant P., Desmaison J., Remote microwave plasma-enhanced chemical vapour deposition of insulating coatings (SiO_2) on metallic substrates: film properties, *Surface and Coatings Technology,* 80 (1996) 18-22.

Roberts David H., Extruded Lead strengthened by dispersed oxide, *GB patent n°970259* (1964).

Subramanian R., Ramachandran S., Electrodeposition of Lead-Tin alloy for Use as Anodes, *Metal Finishing*, (1996) pp.53-56.

Takahashi K., Yasuda Y., Hagegawa H., Horie S., Karatsuki K., Eight years of experience with valve-regulated batteries for automotive use. *J. Power Sources*, 53 (1995) pp.137-141.

Tilman M.M., Crosby R.L., Desy D.H., Dispersion strengthening of lead by coprecipitation, *U.S., Bur. Mines, Rep. Invest* (1971).

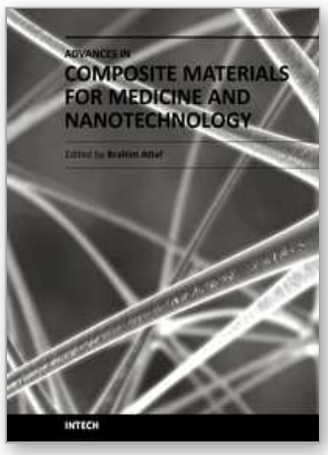

Advances in Composite Materials for Medicine and Nanotechnology

Edited by Dr. Brahim Attaf

ISBN 978-953-307-235-7
Hard cover, 648 pages
Publisher InTech
Published online 01, April, 2011
Published in print edition April, 2011

Due to their good mechanical characteristics in terms of stiffness and strength coupled with mass-saving advantage and other attractive physico-chemical properties, composite materials are successfully used in medicine and nanotechnology fields. To this end, the chapters composing the book have been divided into the following sections: medicine, dental and pharmaceutical applications; nanocomposites for energy efficiency; characterization and fabrication, all of which provide an invaluable overview of this fascinating subject area. The book presents, in addition, some studies carried out in orthopedic and stomatological applications and others aiming to design and produce new devices using the latest advances in nanotechnology. This wide variety of theoretical, numerical and experimental results can help specialists involved in these disciplines to enhance competitiveness and innovation.

InTech Europe
University Campus STeP Ri
Slavka Krautzeka 83/A
51000 Rijeka, Croatia
Phone: +385 (51) 770 447
Fax: +385 (51) 686 166
www.intechopen.com

InTech China
Unit 405, Office Block, Hotel Equatorial Shanghai
No.65, Yan An Road (West), Shanghai, 200040, China
中国上海市延安西路65号上海国际贵都大饭店办公楼405单元
Phone: +86-21-62489820
Fax: +86-21-62489821

IntechOpen